JOURNAL OF APPLIED CRYSTALLOGRAPHY
ISSN 1600-5767

A radially accessible tubular *in situ* X-ray cell for spatially resolved *operando* scattering and spectroscopic studies of electrochemical energy storage devices

Hao Liu,[a] Phoebe K. Allan,[b] Olaf J. Borkiewicz,[a] Charles Kurtz,[a] Clare P. Grey,[b] Karena W. Chapman[a]* and Peter J. Chupas[a]*

[a]X-ray Science Division, Advanced Photon Source, Argonne National Laboratory, 9700 South Cass Avenue, Argonne, IL 60439, USA, and [b]Department of Chemistry, University of Cambridge, Lensfield Road, Cambridge CB2 1EW, UK. *Correspondence e-mail: chapmank@aps.anl.gov, chupas@aps.anl.gov

Received 9 June 2016
Accepted 4 August 2016

Edited by Th. Proffen, Oak Ridge National Laboratory, USA

Keywords: *in situ* X-ray electrochemical cells; energy storage; batteries; capacitors; spatial resolution.

A tubular *operando* electrochemical cell has been developed to allow spatially resolved X-ray scattering and spectroscopic measurements of individual cell components, or regions thereof, during device operation. These measurements are enabled by the tubular cell geometry, wherein the X-ray-transparent tube walls allow radial access for the incident and scattered/transmitted X-ray beam; by probing different depths within the electrode stack, the transformation of different components or regions can be resolved. The cell is compatible with a variety of synchrotron-based scattering, absorption and imaging methodologies. The reliability of the electrochemical cell and the quality of the resulting X-ray scattering and spectroscopic data are demonstrated for two types of energy storage: the evolution of the distribution of the state of charge of an Li-ion battery electrode during cycling is documented using X-ray powder diffraction, and the redistribution of ions between two porous carbon electrodes in an electrochemical double-layer capacitor is documented using X-ray absorption near-edge spectroscopy.

1. Introduction

Electrochemical energy storage devices, such as Li-ion batteries and supercapacitors, are complex, with coupled chemical, electronic and structural processes that occur over multiple length scales. While the active material, embedded within the electrode, governs the fundamental chemistry underlying energy storage, the architecture of the whole device, including the composite electrode structure and the transport properties of the electrode, separator and electrolyte, plays a critical role in realizing its full power and energy (Fongy *et al.*, 2011). Accordingly, to optimize the performance of the active material within a real electrochemical cell, it is valuable to understand how reactions progress through the electrode and how they can be influenced by the cell architecture.

In situ X-ray scattering and spectroscopic measurements provide valuable insights into the structural, chemical, oxidation state and compositional changes that can occur during electrochemical cycling of energy storage materials (Morcrette *et al.*, 2002; Ouvrard *et al.*, 2013). However, most electrochemical cells that have been developed for X-ray-based characterization during cycling are derived from the standard coin cell device that is widely used for electrochemical testing (Borkiewicz *et al.*, 2012; Herklotz *et al.*, 2013; Leriche *et al.*, 2010; Balasubramanian *et al.*, 2001; Farley, 1999;

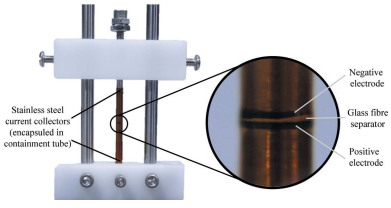

Nikolowski *et al.*, 2005; Richard, 1997). In a coin cell, thin disc-shaped layers of electrodes are stacked, separated by an electrolyte-soaked ion-permeable membrane. In *in situ* studies, the high aspect ratio of this multilayer architecture (~1 cm in diameter but ~0.1 cm thick) favours measurements with the incident beam directed perpendicular to the layers. In this measurement geometry, all layers within the device are probed simultaneously, such that the measured data include contributions from the positive and negative electrodes, the separator, and the electrolyte. The signal from individual components or depths within a component cannot be deconvoluted.

This standard measurement geometry does not allow us to use *in situ* studies to understand inhomogeneities that may develop within the electrode layer or changes in electrodes of similar structure (*i.e.* the high surface energy carbons that make up both the positive and negative electrodes in capacitors). Inhomogeneities along the electrode stacking direction have been shown to be related to the architecture of the electrode, such as porosity (Strobridge *et al.*, 2015; Robert *et al.*, 2013). Hence, measurements to resolve how the reaction progresses along the stacking direction can provide important insights into the structure–performance relationship in electrochemical energy storage devices.

Alternative measurement geometries and modalities are needed to spatially resolve the transformation within the electrode perpendicular to the layer. While *post mortem* mapping of the electrode stack recovered from a cycled battery can resolve inhomogeneities along the stacking direction (Borkiewicz *et al.*, 2013), this provides limited insight into the kinetics and dynamic nature of such effects. Such *ex situ* studies cannot be applied to separate the signal from carbon electrodes in capacitors.

Specialized measurement modalities can recover depth-resolved information using a coin-cell type sample environment. Specifically, in energy-dispersive X-ray diffraction (EDXRD), spatially resolved data, as a function of depth within the cell, can be obtained by using a slit in the diffracted beam to isolate the signal from a selected volume within the cell, with a full diffraction pattern collected as a function of X-ray beam energy rather than of scattering angle (Giessen & Gordon, 1968). A map of all cell components can be achieved by changing the slit position (Strobridge *et al.*, 2015; Takeuchi *et al.*, 2013). However, application of EDXRD is limited to diffraction studies of crystalline materials: spatially resolved measurement from a sample volume defined by a slit cannot be adapted to total scattering or absorption methodologies. Furthermore, EDXRD is best suited to qualitative phase identification rather than full Rietveld structural refinement, owing to challenges in normalizing the measured X-ray scattering intensities.

Recently, alternative electrochemical cell designs have been reported that allow X-ray transmission perpendicular to the electrode stacking direction, such that the individual components can be probed separately and/or mapped. This includes cells based on capillaries (Johnsen & Norby, 2013; Wang *et al.*, 2015) and Swagelok fittings (Ebner *et al.*, 2013). However, these designs use specialized electrode preparations and configurations that deviate substantially from the composite electrodes used in real devices (*e.g.* dip coating of electrode material onto wires). This makes it challenging to correlate observations with phenomena that occur in a real electrochemical cell.

Here, we present a new electrochemical cell for spatially resolved *operando* X-ray scattering and spectroscopic studies that separately probe and map the individual device components. This tubular geometry cell allows X-ray transmission perpendicular to the electrode stack direction. The radially accessible tubular *in situ* X-ray (RATIX) cell is suitable for both X-ray scattering (diffraction, small-angle scattering and total scattering) and X-ray absorption spectroscopies in transmission or fluorescence geometry. It can be readily adapted for tomographic measurements. Quantitative analysis of the data, including Rietveld structural refinement, can be successfully undertaken. Unlike earlier capillary or Swagelok-based electrochemical cell designs, the RATIX cell is compatible with the electrode composition/fabrication and architecture (including stack pressure) used in standard electrochemical cells. Accordingly, the observations can be used to directly inform our understanding of real device function and failure.

The reliability of the electrochemical cell and the quality of the resulting X-ray scattering and spectroscopic data are demonstrated for two types of energy storage system. The evolution of the distribution of the state of charge of an Li-ion battery electrode during cycling is proved using X-ray powder diffraction, and the redistribution of ions between two porous carbon electrodes in an electrochemical double-layer capacitor is documented using X-ray absorption near edge spectroscopy.

2. RATIX cell description

The RATIX cell allows transmission of X-rays in the plane parallel to the electrode stack. For a sufficiently small beam, the X-ray beam can be transmitted through a single component/layer within the electrode stack. The RATIX cell (Fig. 1) has several principal components: the electrode stack, containment tube, two electrode pins, tensioning screw, base and top assembly, and alignment pins.

2.1. Electrode stack

The assembled RATIX cell contains a regular electrode stack (negative electrode, electrolyte-soaked ion-permeable separator and positive electrode) within an X-ray-transparent tube. The components of the electrode stack are prepared with a smaller diameter than typically used in coin cells. The electrodes and separator are prepared as 3 mm diameter discs, to match the 1/8 inch (1 inch = 2.54 cm) inner diameter of the containment tube. The electrode can be either free-standing, as a pellet or self-supported film, or deposited on metal foils. The concentration of active material within the electrode can be tuned to optimize for absorption or scattering, as necessary.

2.2. Containment tube

The X-ray-transparent containment tube provides complete angular access for X-rays in the plane of the electrode stack. Vacuum grease facilitates a seal between the containment tube and the electrode pins. The tube extends far above and below the electrode stack, increasing the surface in contact with the electrode pins and hence providing a more robust hermetic seal of the cell contents.

A polyimide containment tube, of 1/8 inch inner diameter, was used for the RATIX cell. The optical transparency of polyimide helps in visualizing the cell contents and aligning these within the X-ray beam. Other electrically insulating low-absorption or X-ray-transparent chemically inert tubing materials, such as polytetrafluoroethylene (PTFE), could alternatively be used to contain the electrode stack. As the containment tube is in direct contact with both of the electrode pins, electrically conductive materials such as beryllium and glassy carbon, which are often used as X-ray-transparent windows, are unsuitable.

2.3. Electrode pins and tensioning screw

Two electrode pins sandwich the electrode stack within the tube, serving as both current collector and seal (with the containment tube). The ends of the electrode pins are flattened to ensure a uniform pressure is exerted across the electrode stack. The 1/8 inch outer diameter of these precision-ground rods is matched to the inner diameter of the containment tube. The electrode pins are composed of 316-series stainless steel, or could be fabricated from other materials with suitable electrical conductivity and corrosion/chemical resistance (*e.g.* Ni-plated aluminium). The top current collector is in contact with a tensioning screw, which can be used to adjust the stack pressure.

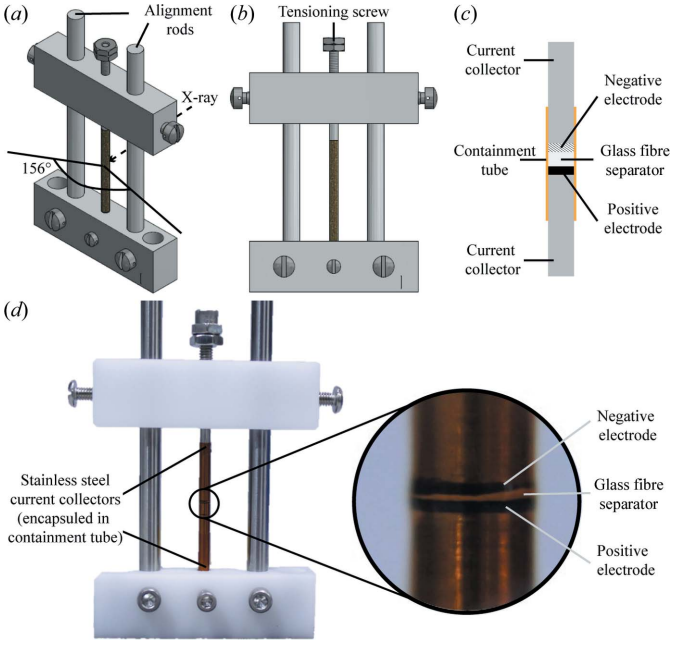

Figure 1
(*a*) and (*b*) Schematic diagrams of the RATIX cell. (*c*) A cross section of the assembled electrode stack sandwiched between current collectors, contained within the polyimide tube. (*d*) A photograph of an assembled RATIX cell, with a magnified region of the electrode stack (inset).

2.4. Base/top pieces and alignment rods

Electrically insulating base and top pieces, connected by two alignment rods, support the containment tube, electrode pins and tensioning screw. The cell base and top piece are fabricated from an electrically insulating mechanically stable polymer [here, Delrin (DuPont)]. The base and top pieces include holes to accommodate the alignment rods and the electrode pins. Threaded holes perpendicular to the alignment/electrode holes allow the base/top pieces to be secured to the alignment rods with screws. Through holes in the base pieces allow mounting of the cell on the instrument.

The alignment rods are 1/4 inch outer diameter precision-ground stainless steel. These rods facilitate alignment and assembly of the cell. In the present cell design, with the rods 5/8 inch away from the electrode stack and alignment tube, the rods define an angular range (*e.g.* for scattering) of 156°. This could be increased by modifying the placement of the alignment rods, replacing the rods with less attenuating hollow tubing or low-Z materials, thinning the alignment rods, or eliminating the alignment rods altogether (if a mechanically stable containment tube is used).

3. RATIX performance

The electrochemical performance of the RATIX cell was demonstrated for a carbon supercapacitor electrode and an $LiNi_{0.8}Co_{0.15}Al_{0.05}O_2$ (NCA) Li-ion battery electrode. X-ray scattering measurements with the RATIX cell were demonstrated for an $LiFePO_4$ electrode, which operates by reversible insertion and extraction of Li while maintaining the $FePO_4$ framework (Padhi, 1997). Application of the RATIX cell for X-ray absorption spectroscopies was demonstrated through cycling of a carbon supercapacitor with a tetraethylammonium bromide ($C_8H_{20}NBr$) electrolyte.

3.1. Electrochemistry

The electrochemical performance of the RATIX cell was benchmarked against standard 2032 coin cells for electrodes prepared using an identical procedure (see §5.2). Cyclic voltammetry (CV) and galvanostatic cycling performed for the carbon-based supercapacitor and NCA electrode, respectively, are shown in Fig. 2.

For the supercapacitor (Fig. 2*a*), the current response in the RATIX cell is slower than in the coin cell, with noticeable differences immediately after switching the voltage polarity. However, when the current starts to plateau, the CV curves become effectively identical.

For galvanostatic cycling, the behaviour of the RATIX cell was compared with two identically prepared coin cells. For the first charge–discharge cycle of NCA (Fig. 2*b*), the charge profiles for both types of cell are almost identical up to 0.2 Li extraction, except with a voltage offset ~20 mV higher for the

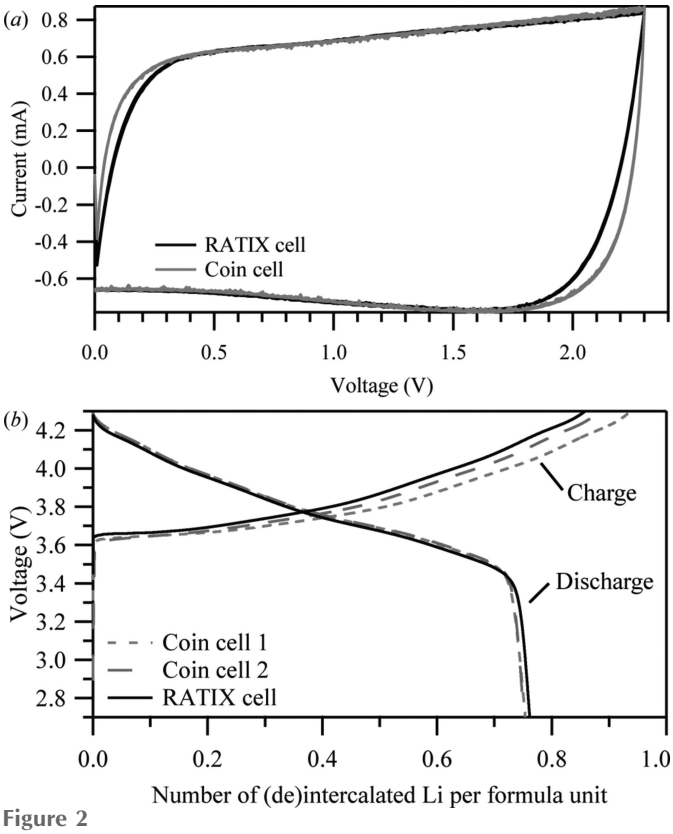

Figure 2
(*a*) Cyclic voltammetry of the supercapacitor electrode measured in the RATIX cell and the coin cell at 1.3 mV s^{-1} in the voltage window 0–2.3 V. (*b*) Charge and discharge voltage profiles of the $LiNi_{0.8}Co_{0.15}Al_{0.05}O_2$ electrode in the RATIX and coin cells at *C*/20 in the voltage window 2.7–4.3 V.

RATIX cell. After 0.2 Li extraction, the charge profiles begin to diverge, not only between the RATIX and coin cells but also between the two coin cells. Therefore, the large differences observed in this regime are introduced by the inevitable variation in the cell preparation conditions (despite the fact that the same protocol has been used). It is known that NCA undergoes an activation process on the first charge (Robert *et al.*, 2015), so the variation in electrochemistry between the different cells may be particularly exacerbated for NCA on the first charge. On discharge, all cells showed almost identical voltage profiles and achieved similar discharge capacities. It is noted that the discharge profile for the RATIX cell is consistently lower than the coin cells by ∼20 mV, which mirrors the ∼20 mV overpotential on charge up to 0.2 Li extraction. The larger polarization is likely to arise from the use of two layers of glass fibre separators (as opposed to one layer in coin cells), which greatly reduces the chance of a short circuit at the cost of increased internal resistance.

3.2. X-ray scattering measurements

The diffraction data measured for the $LiFePO_4$ electrode in the as-assembled RATIX cell are shown in Fig. 3. All reflections can be assigned to the components in the $LiFePO_4$ electrode: in addition to $LiFePO_4$, PTFE and graphite also give rise to intense peaks at 2.5 and 3.6°, respectively. Major contributions to the slowly varying background arise from scattering due to the polyimide tube, electrolyte filling the porous space of the electrode, amorphous carbon in the electrode, and air. The measurement geometry with a greater thickness of the electrode in the beam path than with the coin cell geometry, where the beam is parallel to the electrode stack direction (3 m *cf.* 0.1 mm), yields a larger scattering signal from the sample and an improved signal-to-background ratio. Accordingly, the background is very low compared with the signal from conventional *operando* cells (Leriche *et al.*, 2010). Rietveld refinement can be performed against this data to provide quantitative structural parameters (R_{wp} = 0.063, goodness of fit = 0.94). The excellent goodness of fit is a consequence of the low signal-to-background ratio relative to standard capillary measurement.

4. Applications to an electrochemical double-layer capacitor: *operando* X-ray absorption spectroscopy

4.1. Electrochemical double-layer capacitors

Electrochemical double-layer capacitors (EDLCs) store charge through the reversible adsorption of ions of the electrolyte onto the surface of an active electrode material, which is electrochemically stable and has a high specific surface area. As no redox reaction occurs during EDLC operation, when a voltage difference is applied between the two electrodes, the positively and negatively charged ions of the electrolyte accumulate at the negative and the positive electrodes, respectively, forming charged double layers.

In supercapacitor devices, both the positive and negative electrodes are essentially the same material – a high surface area carbon. In conventional geometries for synchrotron X-ray characterization, the signals from each electrode cannot be readily distinguished.

X-ray absorption spectroscopy was used to evaluate the migration of the electrolyte ions and their adsorption within the electrodes. Using tetraethylammonium bromide

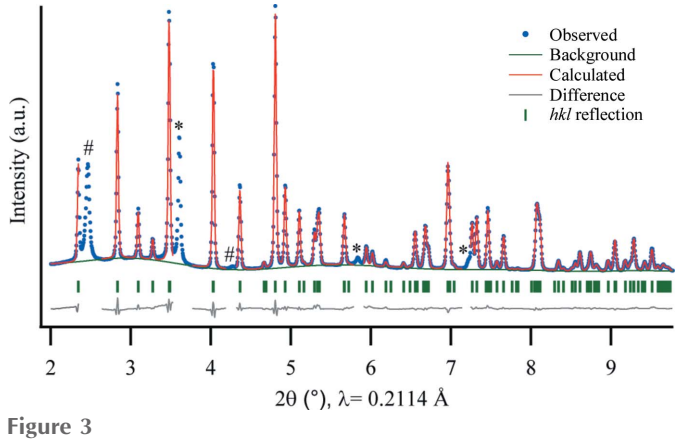

Figure 3
Rietveld refinement against the diffraction data collected for the $LiFePO_4$ electrode in the assembled RATIX cell. Scattering features from PTFE and graphite are indicated by # and * symbols, respectively, and are excluded from the refinement.

($C_8H_{20}NBr$) electrolyte, Br *K*-edge X-ray absorption near-edge structure (XANES) measurements allowed the spatial distribution of Br^- through the electrode stack to be evaluated at different applied voltages.

4.2. Experimental details

Supercapacitor electrodes were prepared as films. A mixture of 95 wt% YP-50 carbon (Kuraray Chemical Co., Japan) and 5 wt% PTFE binder (60% dispersion in water, Sigma–Aldrich) was suspended in ethanol and heated at 343 K for 1 h with ethanol being replenished. The ethanol was then removed by heating and the resultant paste was kneaded and rolled into a film of 0.5 mm thickness. Electrodes of 3 mm diameter were cut from the film and dried at 378 K under vacuum overnight before use. The electrodes were assembled in an argon glovebox in the cell using a Whatman GF/B glass fibre separator, with approximately 5 µl of tetraethylammonium bromide (>99%, Sigma–Aldrich) in acetonitrile (anhydrous, 99.8%, Sigma–Aldrich) solution as electrolyte. A voltage was applied across the cell and the current was allowed to decay to steady state before the data collection was started.

The Br *K*-edge XANES measurements were carried out on beamline 11-ID-D at the Advanced Photon Source, Argonne National Laboratory, using a 30 µm vertical beam size at spacings of 30 µm. Spectra were measured in transmission geometry using two ion chambers. Data were analysed using *Athena* (Ravel & Newville, 2005).

4.3. Results

The XANES spectra were measured at different positions through the electrode stack when a constant voltage was applied between the electrodes (see Fig. 4). As the absorption is normalized, a higher absorption contrast at the absorption edge corresponds to a higher Br^- concentration. When there is no voltage difference between the electrodes, *i.e.* at 0 V as shown in Fig. 4(*a*), the Br^- concentration is equal at both electrodes; at 0 V there is no preference for the negative Br^- ions to adsorb onto one electrode over the other. When a voltage difference of 600 mV is applied between the electrodes (Fig. 4*b*), a higher Br^- concentration is observed at the positive than the negative electrode. A further increase in the voltage difference to 1200 mV (Fig. 4*c*) increases the difference in the Br^- concentration between the electrodes. The observed increase in Br^- concentration at the positive electrode with increasing voltage is consistent with the charge storage mechanism of EDLCs.

5. Applications to evaluate the composition variation through an Li-ion battery electrode by X-ray diffraction

5.1. Heterogeneous reactions in Li-ion battery electrodes

Lithium-ion battery operation requires transport of lithium ions from one electrode to the other, across an ion-permeable membrane. The three-dimensional architecture of the composite electrode, which includes the active material, conductive carbon and polymer binder, provides conduction pathways for both ion transport and electrical conductivity. Accordingly, the electrode architecture can strongly impact the performance of a battery.

Since a concentration gradient is required to drive the Li diffusion from one electrode to the other, it can be envisaged that the state of charge (SOC) of the active material particles will vary along the Li concentration gradient. Previous *operando* (Strobridge *et al.*, 2015) and *post mortem* (Robert *et al.*, 2013) studies have shown the variation in the SOC through an

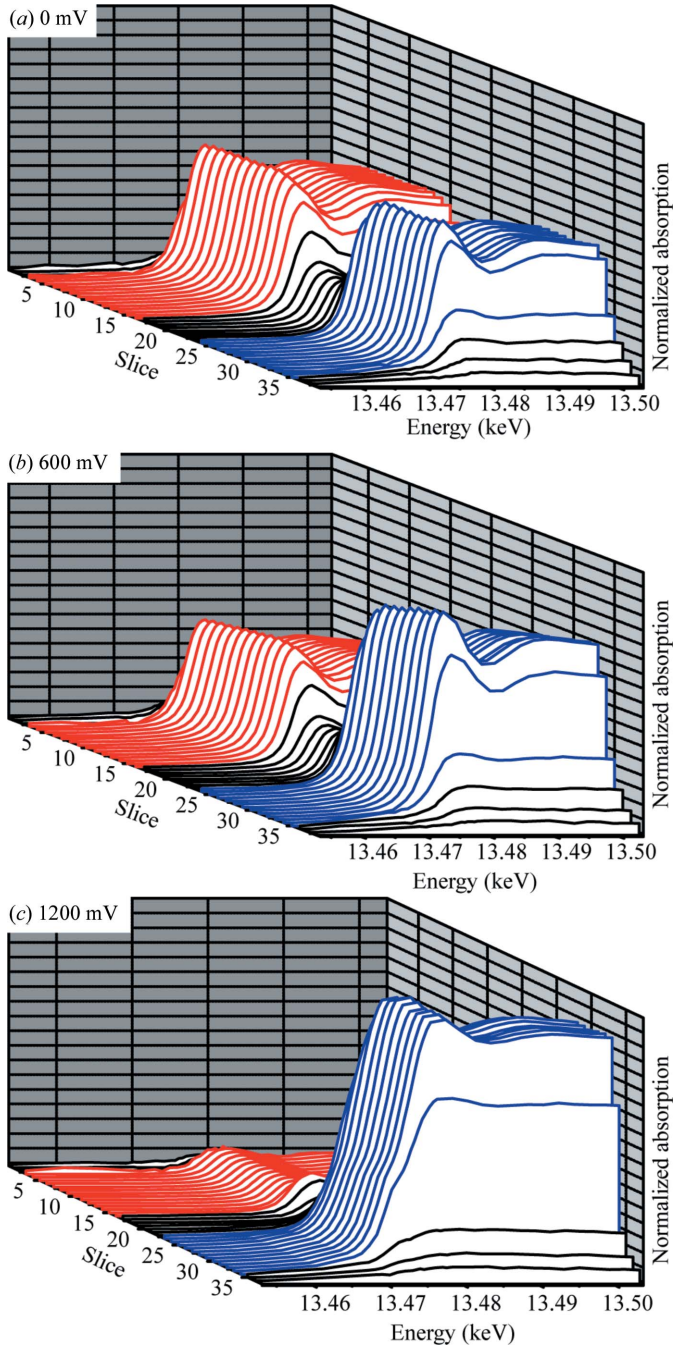

Figure 4
Br *K*-edge XANES spectra measured at 30 µm steps through the electrode stack. Data are shown for (*a*) 0 mV, (*b*) 600 mV and (*c*) 1200 mV applied potential difference between the negative (red) and positive (blue) electrodes.

$LiFePO_4$ composite electrode. To understand how the architecture of the electrode affects the rate performance, characterization tools that can directly probe the SOC through the electrode are needed. The potential for using the RATIX cell to probe how the SOC evolves within an electrode is demonstrated by mapping through the $LiFePO_4$ electrode during *operando* electrochemical cycling. As the cycling of the $LiFePO_4$ electrode proceeds by varying the relative fraction of $LiFePO_4$ and $FePO_4$, the relative phase fraction of $FePO_4$ is directly proportional to, and can be used as a measure of, the SOC.

5.2. Experimental details

Composite electrodes of active material ($LiFePO_4$ or $LiNi_{0.8}Co_{0.15}Al_{0.05}O_2$ for §3.1) were prepared as pellets. In a typical setup, active electrode material was mixed with 'Super P' carbon (Alfa Aesar), carbon black (Vulcan XC-72, Cabot Corporation) and PTFE binder (Sigma–Aldrich) in a mass ratio of 6:1:1:2 (total mass ~4 mg) and the mixture was formed into pellets (3 mm diameter, 200–300 µm thick, applied loads of 1/8 ton). The electrode pellets were assembled into the cells with a glass fibre separator (Whatman), Li metal foil (Aldrich) and liquid electrolyte solution (1 *M* $LiPF_6$ in 1:1 ethylene carbonate/dimethyl carbonate, from Tomiyama Pure Chemical Industries). Cells were cycled galvanostatically against lithium at rates of *C*/2 and 2*C* in a voltage window of 2–4.5 V, where *C*/*x* corresponds to the current used to (dis)charge to full capacity in *x* hours.

X-ray scattering data were collected at the Advanced Photon Source at Argonne National Laboratory using beamline 11-ID-B (λ = 0.2114 Å), equipped with an amor-

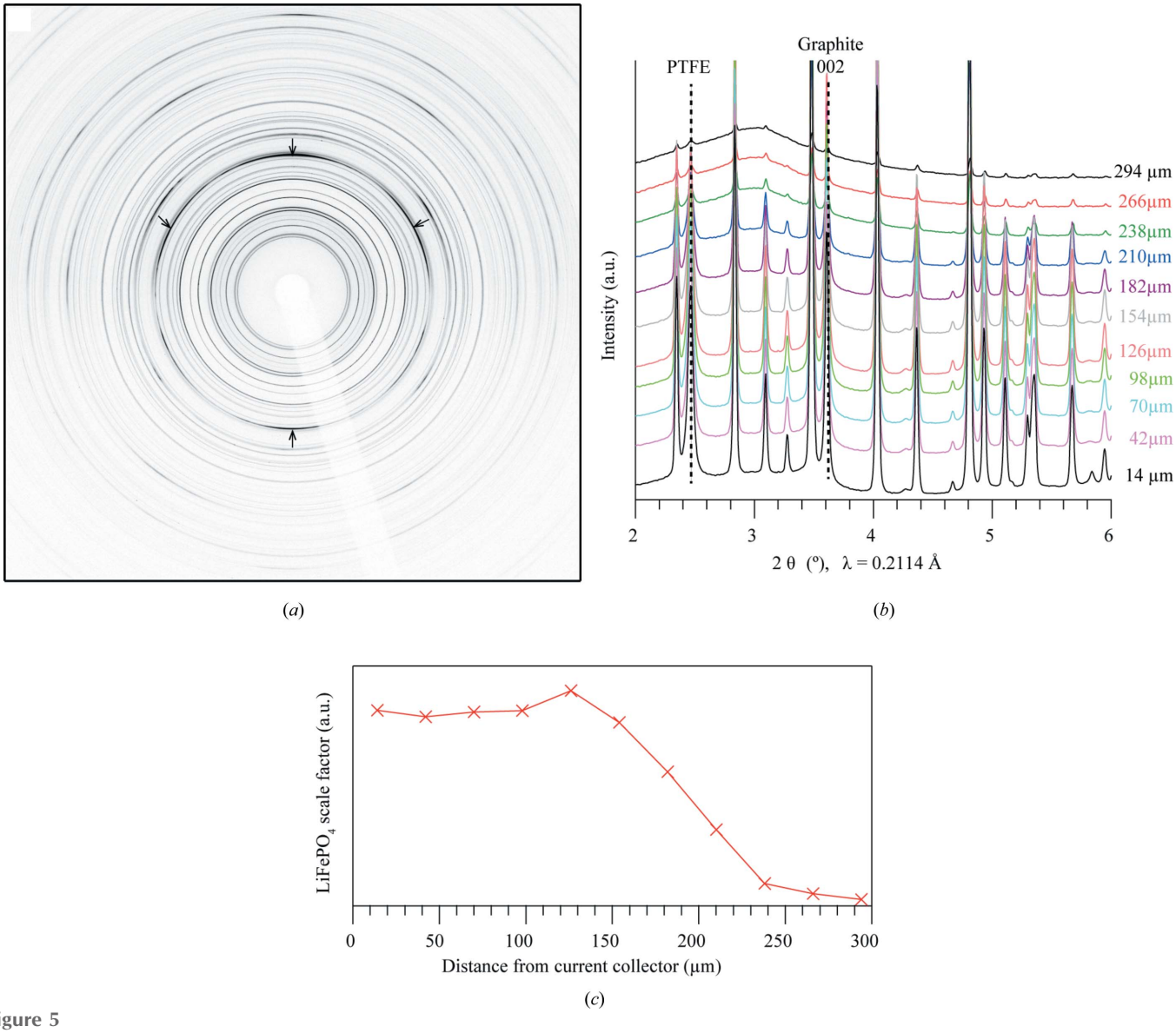

Figure 5
(*a*) A raw diffraction image at a position close to the current collector. Typical streaks corresponding to the stainless steel current collector are indicated by arrows. (*b*) XRD patterns measured at different positions through the $LiFePO_4$ electrode. (*c*) The scale factor obtained from the Rietveld refinement against the patterns collected before cycling.

phous silicon-based area detector from Perkin–Elmer. The use of high-energy X-rays minimizes absorption effects. The detector was positioned at a distance of 95 cm from the sample.

The RATIX cell was oriented vertically with the electrode of interest at the bottom. To increase the mapping resolution, the size of the beam was reduced to 20 µm in the stack (vertical) direction, but remained large (500 µm) in the perpendicular (horizontal) direction. The acquisition time for each diffraction pattern was 1 s, and diffraction patterns were measured consecutively at 11 positions from the separator to the current collector side (top to bottom) of the electrode in steps of 28 µm. Including the time needed to move the sample vertically, each series of measurements across the electrode took 35 s. The series of measurements was repeated during the electrochemical cycling of the $LiFePO_4$ electrode.

Rietveld refinement against the $LiFePO_4$ data was performed sequentially using the *TOPAS* software package (Coelho, 2012). Since the electrochemical cycling proceeds *via* a change in the proportions of $LiFePO_4$ and $FePO_4$, the structural parameters (atomic coordinates and atomic displacement parameters) for $LiFePO_4$ and $FePO_4$ were first determined from full refinement of data collected before and at the end of charge, then fixed for the sequential refinement. In the sequential refinement, only the lattice parameters, peak profile (isotropic size and strain broadening) and phase fraction were refined.

5.3. Mapping the $LiFePO_4$ electrode by X-ray diffraction in an as-assembled RATIX cell

Owing to the finite beam size and the direct contact between the $LiFePO_4$ electrode and the current collector, X-ray diffraction (XRD) data collected at positions near the bottom of the electrode include contributions from the electrode pin or current collector (Fig. 5*a*). Diffraction intensities corresponding to the current collector are observed as arcs rather than complete rings in the two-dimensional scattering image. For this mapping experiment, only data without scattering contributions from the electrode pins were analysed, the closest distance between the centre of beam and the flat surface of the current collector being 14 µm (the vertical beam width is 20 µm).

A consequence of the probe volume being near the current collector is that the scattering image is asymmetric about the horizontal plane: the beam scattered down is partially attenuated by the electrode pin and, as a result, appears to have a lower intensity than the beam scattered up. The effect of absorption can be mitigated by basing the analysis on data from the un-attenuated top half of the image only.

Diffraction data collected at different positions through the electrode layer are shown in Fig. 5(*b*). All Bragg reflections can be indexed to $LiFePO_4$, except for the PTFE and graphite peaks indicated by the dashed black lines. A progressive decrease in $LiFePO_4$ diffraction intensities was observed for positions above ∼150–175 µm, suggesting a graduated interface between the electrode and separator, possibly due to roughness in the electrode surface or tilting of the electrode surface relative to the X-ray beam. To quantify the $LiFePO_4$ variation through the electrode, the $LiFePO_4$ scale factor, which is proportional to the absolute amount of this phase, was obtained from the Rietveld refinements (Fig. 5*c*). The amount of $LiFePO_4$ remains constant up to ∼150–175 µm, after which it starts to decrease. At each position above 230 µm, the absolute amount of $LiFePO_4$ is only 10% of that below 100 µm. The very small amount of electrode material above 230 µm could be due to small (probably disconnected) electrode fragments.

5.4. *In situ* XRD measurement of the $LiFePO_4$ electrode during electrochemical cycling

The charge and discharge of $LiFePO_4$ involves a change in the ratio of $LiFePO_4$ and $FePO_4$. Rietveld refinement was undertaken to quantify the relative phase fraction of $FePO_4$ during charge and discharge. The variation in the $FePO_4$ phase fraction through the electrode at selected SOCs, for cycling rates of *C*/2 and 2*C*, is shown in Fig. 6. The phase fraction of $FePO_4$ changes non-monotonically through the electrode during charge. For example, for 20% SOC during *C*/2 charge (Fig. 6*a*), the $FePO_4$ phase fraction first increases from 0.2 at 14 µm to 0.28 at 182 µm and then decreases to 0.17 at 294 µm. A similar phase-fraction profile is also observed for other SOCs (see Fig. 6*a*). The phase-fraction profile below 200 µm,

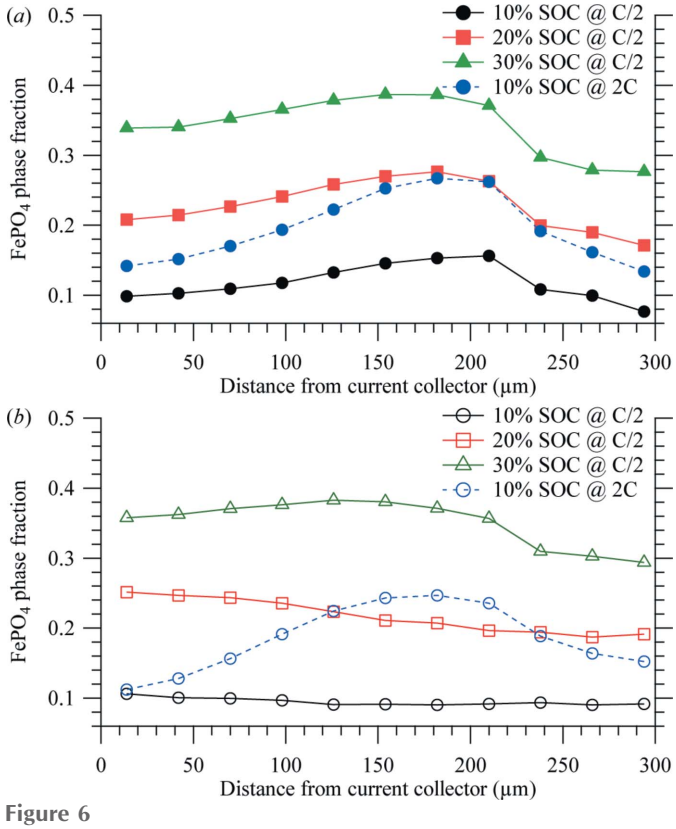

Figure 6
Variation of the $FePO_4$ phase fraction through the electrode at different states of charge (SOCs) during (*a*) the charging and (*b*) the discharging cycle.

where the reaction in the electrode near the separator is more advanced than near the current collector, is consistent with a previous study using EDXRD (Strobridge *et al.*, 2015). The increase in the $LiFePO_4$ phase fraction above 230 µm could be related to the poor electrical conductivity of the electrode segment at this particular position, but understanding the mechanism that leads to such an observation is outside the scope of this paper. When the rate of cycling increases to 2*C*, the phase-fraction gradient below and above 230 µm becomes steeper than that at *C*/2. On discharge, the gradient of the $FePO_4$ phase fraction is reversed from positive to negative from 30% to 20% SOC for a cycling rate of *C*/2, consistent with the observation made on charge. In contrast, the $FePO_4$ phase-fraction profile for 2*C* discharge at 10% SOC resembles that on charge. These differences between charge and discharge, as well as between different cycling rates, can be readily discerned in Fig. 7, which shows the evolution of the $FePO_4$ phase fraction through the electrode during the entire charge and discharge cycle. It is noted that the phase-fraction profile on discharge is different from that on charge for *C*/2 cycling, whereas the phase-fraction profile on discharge almost mirrors that on charge for 2*C* cycling.

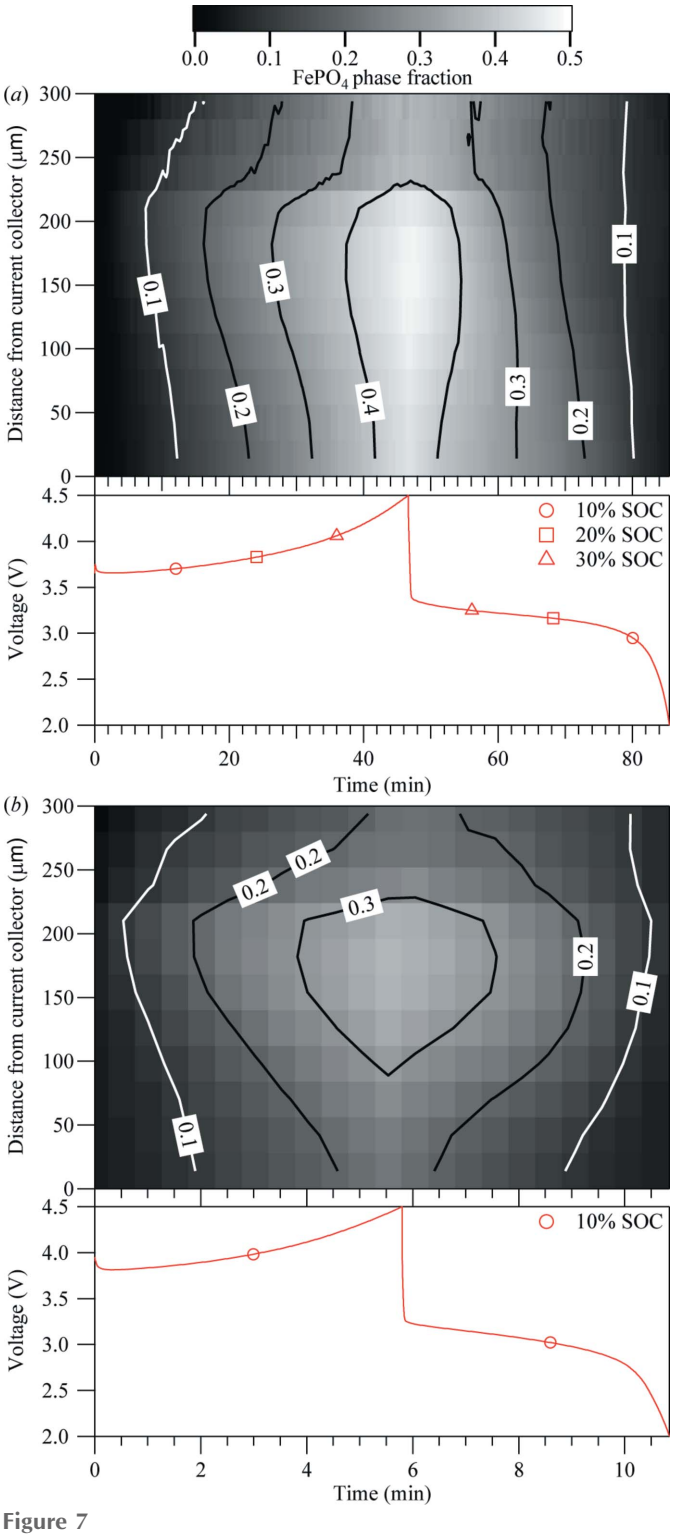

Figure 7
The evolution of the $LiFePO_4$ phase fraction as a function of time and position during charge and discharge at cycling rates of (*a*) *C*/2 and (*b*) 2*C*. The $LiFePO_4$ phase fraction is represented in greyscale and contour lines are drawn from 60 to 90% phase fraction in 10% increments. The corresponding voltage profiles are also shown.

The electrochemical capacity utilized here, with only 40 and 20% of the theoretical capacity achieved at cycling rates of *C*/2 and 2*C*, respectively, reflects the fact that the $LiFePO_4$ particles were not coated with a conductive layer. Conductive coating of electrode particles is critical to realizing the high rate performance of $LiFePO_4$ (Huang *et al.*, 2001; Ravet *et al.*, 2001). Here, the low capacity utilization (>80% capacity utilization is usually achieved at 2*C*) and the high voltage polarization (*i.e.* the voltage difference between charge and discharge in the plateau region) observed can be attributed to the inherently poor electronic conductivity of the present $LiFePO_4$ particles.

6. Conclusions

The RATIX cell, which can separately probe and map individual components within an operating electrochemical cell, complements existing *operando* cells used to investigate the structural and chemical changes in the electrode as a whole. It can be particularly valuable for understanding phenomena that occur at the electrode level. As demonstrated for the two examples presented here, the RATIX cell can be readily integrated into X-ray scattering and absorption instruments. Although not presented here, the wide angular access of this cell is also compatible with X-ray tomography, which can be used to visualize the electrode architecture in three dimensions. Using the RATIX cell, it should be possible to perform *in situ* tomographic measurements to image the entire electrode layer/stack in three dimensions during battery operation. The use of the RATIX cell provides new ways to characterize the structure–performance relationship, the understanding of which is crucial in developing high energy and power density electrochemical energy storage devices.

Acknowledgements

This research was supported as part of the NorthEast Center for Chemical Energy Storage (NECCES), an Energy Frontier

Research Center funded by the US Department of Energy, Office of Science, Office of Basic Energy Sciences, under award No. DE-SC0012583. This research used resources of the Advanced Photon Source, a US Department of Energy (DOE) Office of Science User Facility operated for the DOE Office of Science by Argonne National Laboratory under contract No. DE-AC02-06CH11357. PKA acknowledges a Junior Research Fellowship from Gonville and Caius College and an Oppenheimer Fellowship from the University of Cambridge. The authors thank Elizabeth K. Humphreys for useful discussions.

References

Balasubramanian, M., Sun, X., Yang, X. Q. & McBreen, J. (2001). *J. Power Sources*, **92**, 1–8.
Borkiewicz, O. J., Chapman, K. W. & Chupas, P. J. (2013). *Phys. Chem. Chem. Phys.* **15**, 8466–8469.
Borkiewicz, O. J., Shyam, B., Wiaderek, K. M., Kurtz, C., Chupas, P. J. & Chapman, K. W. (2012). *J. Appl. Cryst.* **45**, 1261–1269.
Coelho, A. (2012). *TOPAS*. Coelho Software, Brisbane, Australia.
Ebner, M., Marone, F., Stampanoni, M. & Wood, V. (2013). *Science*, **342**, 716–720.
Farley, N. R. S. (1999). *Electrochem. Commun.* **1**, 449–452.
Fongy, C., Jouanneau, S., Guyomard, D. & Lestriez, B. (2011). *J. Power Sources*, **196**, 8494–8499.
Giessen, B. C. & Gordon, G. E. (1968). *Science*, **159**, 973–975.
Herklotz, M., Scheiba, F., Hinterstein, M., Nikolowski, K., Knapp, M., Dippel, A.-C., Giebeler, L., Eckert, J. & Ehrenberg, H. (2013). *J. Appl. Cryst.* **46**, 1117–1127.
Huang, H., Yin, S. C. & Nazar, L. F. (2001). *Electrochem. Solid State Lett.* **4**, A170–A172.
Johnsen, R. E. & Norby, P. (2013). *J. Appl. Cryst.* **46**, 1537–1543.
Leriche, J. B., Hamelet, S., Shu, J., Morcrette, M., Masquelier, C., Ouvrard, G., Zerrouki, M., Soudan, P., Belin, S., Elkaïm, E. & Baudelet, F. (2010). *J. Electrochem. Soc.* **157**, A606–A610.
Morcrette, M., Chabre, Y., Vaughan, G., Amatucci, G., Leriche, J. B., Patoux, S., Masquelier, C. & Tarascon, J. M. (2002). *Electrochim. Acta*, **47**, 3137–3149.
Nikolowski, K., Baehtz, C., Bramnik, N. N. & Ehrenberg, H. (2005). *J. Appl. Cryst.* **38**, 851–853.
Ouvrard, G., Zerrouki, M., Soudan, P., Lestriez, B., Masquelier, C., Morcrette, M., Hamelet, S., Belin, S., Flank, A. M. & Baudelet, F. (2013). *J. Power Sources*, **229**, 16–21.
Padhi, A. K. (1997). *J. Electrochem. Soc.* **144**, 1188–1194.
Ravel, B. & Newville, M. (2005). *J. Synchrotron Rad.* **12**, 537–541.
Ravet, N., Chouinard, Y., Magnan, J. F., Besner, S., Gauthier, M. & Armand, M. (2001). *J. Power Sources*, **97–98**, 503–507.
Richard, M. N. (1997). *J. Electrochem. Soc.* **144**, 554–557.
Robert, D., Douillard, T., Boulineau, A., Brunetti, G., Nowakowski, P., Venet, D., Bayle-Guillemaud, P. & Cayron, C. (2013). *ACS Nano*, **7**, 10887–10894.
Robert, R., Bünzli, C., Berg, E. J. & Novák, P. (2015). *Chem. Mater.* **27**, 526–536.
Strobridge, F. C., Orvananos, B., Croft, M., Yu, H. C., Robert, R., Liu, H., Zhong, Z., Connolley, T., Drakopoulos, M., Thornton, K. & Grey, C. P. (2015). *Chem. Mater.* **27**, 2374–2386.
Takeuchi, E. S., Marschilok, A. C., Takeuchi, K. J., Ignatov, A., Zhong, Z. & Croft, M. (2013). *Energ. Environ. Sci.* **6**, 1465–1470.
Wang, J., Eng, C., Chen-Wiegart, Y. C. & Wang, J. (2015). *Nat. Commun.* **6**, 7496.